Sensors & Diagnostics

PAPER

View Article Online
View Journal | View Issue

Cite this: *Sens. Diagn.*, 2023, **2**, 699

Preparation of Z-scheme 3D ZnO/Au/g-C_3N_4 heterostructures for the photoelectrochemical sensing of glutathione†

Weixin Li,[a] Xinyang Wang,[a] Jiaji Huang,[b] Min Zhao,*[cd] Jiao Yang,[a] Fang Luo,[a] Bin Qiu,[a] Jian Wang *[a] and Zhenyu Lin *[a]

Received 13th February 2023,
Accepted 28th March 2023

DOI: 10.1039/d3sd00040k

rsc.li/sensors

Three-dimensional (3D) ZnO nanostructures were used as the support for gold nanoparticles (AuNPs) and graphite carbon nitride (g-C_3N_4) to form a Z-scheme heterostructure photoelectrode (3D ZnO/Au/g-C_3N_4) in this work. The 3D structure of the ZnO nanorods provided a directional channel for fast carrier transport and abundant reaction sites. ZnO and g-C_3N_4 formed the Z-scheme heterojunction, and the AuNPs sandwiched between ZnO and g-C_3N_4 acted as the mediators and greatly reinforced vector electron transfer in the Z-scheme heterojunction. Then, the 3D ZnO/Au/g-C_3N_4 photoelectrode was applied to develop a sensitive photoelectrochemical (PEC) biosensor for reduced glutathione (GSH) detection. GSH can act as a hole scavenger and reduce the recombination of photogenerated electron–hole pairs, which results in an increase in the photocurrent of the system. The enhanced current showed good linearity with GSH concentration in the range of 7–2000 μM, and the system had a limit of detection of 2.3 μM. The proposed biosensor exhibited good selectivity and reproducibility, obtaining satisfactory results in the analysis of the target in human serum.

Introduction

The photoelectrochemical (PEC) detection technique has the characteristics of high sensitivity, low background and simple equipment.[1] Photoactive substances that act as transducers to convert light into electrical signal form an essential component in the development of PEC biosensors.[1,2] Zinc oxide (ZnO) is a kind of n-type semiconductor with a wide bandgap, and the advantages of high electron mobility and morphological plasticity, as well as low cost, low toxicity and ease of preparation.[3] Low-dimensional ZnO nanostructures can provide fast charge transport through micron-scale axial lengths, enabling effective charge separation across nanoscale diameters.[4,5] Compared with simple low-dimensional structures, three-dimensional (3D) ZnO nanostructures not only inherit excellent properties but also exhibit a large surface-area-to-volume ratio and better permeability, which facilitate enhanced light capture, more reactive sites, and faster electron and ion transport capability, due to which they have been applied in the development of PEC biosensors frequently.[6] For instance, Ren's group prepared different structures of ZnO, such as nanotrees, nanorod clusters and parent nanorods, by electrodeposition and hydrothermal growth.[7] In terms of PEC water-splitting performance, they found that the strongest material was the nanotree, while the weakest was the parent nanorod. The key reason for improved performance is the very large surface-to-volume ratios in the branched 3D nanostructures.

Single photoactive materials always exhibit low photoelectric response signals due to the rapid recombination of photogenerated electron–hole pairs, which is easily disturbed by the environment or the substrate, subsequently affecting the accuracy of the detection results. The construction of heterojunctions can address this concern easily.[8,9] Graphite carbon nitride (g-C_3N_4) is a kind of photocatalyst with a unique structure, small interlayer distance and a bandgap of 2.7 eV, which can be driven by

[a] *Ministry of Education Key Laboratory for Analytical Science of Food Safety and Biology, Fujian Provincial Key Laboratory of Analysis and Detection for Food Safety, College of Chemistry, Department of Chemistry, Fuzhou University, Fuzhou, Fujian, 350116, China. E-mail: jwang@fzu.edu.cn, zylin@fzu.edu.cn*
[b] *Clinical Medicine Major, School of Medicine, Xiamen University, Xiamen, Fujian 361005, China*
[c] *Department of Gynecology and Obstetrics, The First Affiliated Hospital of Xiamen University, School of Medicine, Xiamen University, Xiamen, Fujian, 361005, China. E-mail: xmzmdyyy@xmu.edu.cn*
[d] *Computer Management Center, The First Affiliated Hospital of Xiamen University, School of Medicine, Xiamen University, Xiamen, Fujian, 361005, China*

† Electronic supplementary information (ESI) available: Additional experimental details on the characterization of the prepared materials, such as EDX testing of 3D ZnO/Au/g-C_3N_4, XRD testing of various components, XPS testing of 3D ZnO/Au/g-C_3N_4, UV-vis absorption testing of various components, UV-vis diffuse reflectance and UPS measurement of 3D ZnO and g-C_3N_4. See DOI: **https://doi.org/10.1039/d3sd00040k**

visible light.[10–12] Due to its well-matched band edge position with ZnO, g-C_3N_4 has been applied to prepare ZnO/g-C_3N_4 heterojunction systems previously.[13] For example, Bian's group prepared a ZnO/g-C_3N_4 heterojunction photocatalyst, and it was applied for H_2O_2 production under sunlight irradiation.[14] Its H_2O_2 productivity was approximately 2.7 times greater than that on bare g-C_3N_4, which benefited from the construction of the heterojunction.

Z-Scheme heterojunctions consist mostly of two semiconductors and an electron dielectric made of a noble metal. Under sunlight irradiation, light-induced electrons on the conduction band (CB) of one semiconductor migrate to the electron dielectric and subsequently recombine with the light-induced holes on the valence band (VB) of the other semiconductor, which has a relatively strong redox and efficient charge transfer abilities.[8,15,16] Gold nanoparticles (AuNPs) with localized surface plasmon resonance (LSPR) can form Schottky junctions with semiconductor materials. The presence of AuNPs not only broadens the light-absorption range to the visible region but also suppresses the complexation of electron–hole pairs, thereby enhancing the intensity of the photoelectronic signal.[17] Earlier studies have shown that AuNPs sandwiched in ternary heterojunctions can act as mediators to increase the vector mobility of the photogenerated electron–hole pairs.[18] For instance, Li's group facilitated charge transfer from ZnO-based photoanodes and improved the PEC cell conversion efficiency by immobilizing Au-core CdS-shell nanostructures (Au@CdS) on ZnO nanowires, wherein the Au core formed unique nano-junctions with CdS and ZnO.[19] Zou's group[20] constructed a ternary $BiVO_4$–Au–Cu_2O heterostructure by anchoring the Au–Cu_2O composite structure on the face of the truncated $BiVO_4$ octahedron. The synthesized $BiVO_4$–Au–Cu_2O could activate inert $BiVO_4$ and Cu_2O and exhibited increased CO_2 reduction activity, which was 5 times greater than that of $BiVO_4$–Cu_2O. However, to the best of our knowledge, AuNPs have never been sandwiched in 3D ZnO and g-C_3N_4 to enhance the performance of the 3D ZnO/Au/g-C_3N_4 Z-scheme heterostructure photoelectrode.

Reduced glutathione (GSH) is one of the antioxidants that are widely present in the body. Abnormal GSH levels are closely associated with a variety of diseases, such as Alzheimer's disease and cardiovascular diseases.[21,22] GSH can act as a hole scavenger, producing electrons that effectively prevent the rapid compounding of photogenerated electron–hole pairs.[23] In this study, 3D ZnO nanostructures have been used as the body to support AuNPs and g-C_3N_4 to form a Z-scheme heterostructure photoelectrode (3D ZnO/Au/g-C_3N_4). This structure combines the advantage of each component and allows efficient electron–hole separation, resulting in a strong PEC photocurrent, as detected. The presence of GSH causes a change in the photocurrent intensity of the system, and the relationship between GSH and the photocurrent is established in this work. Based on this, a sensitive PEC biosensor for GSH can be developed.

Experimental sections

Reagents and instruments

Complete information on the reagents and instrumentations used in this experiment is shown in the ESI.†

Preparation of the photoelectrodes

The procedures employed for the preparation of materials to fabricate 3D ZnO/Au/g-C_3N_4 have been shown in ESI.† The indium tin oxide (ITO) electrodes were cleaned with acetone, ethanol, and deionized water, respectively, by ultrasonication and blown dry with N_2. 20 μL of a 2.0 mg mL^{-1} 3D ZnO/Au/g-C_3N_4 solution was applied dropwise to the ITO electrode by drop-casting and dried in the air. Then, it was used as the photoelectrode for PEC testing.

The procedure of GSH detection

A pre-configured GSH solution was added to the electrolyte solution and mixed thoroughly. The photocurrent signal was detected using a xenon lamp as the excitation light source with a switching frequency of 10 s and an applied voltage of 0.6 V. The PEC test results were quantified by calculating the average of three independent parallel tests.

Results and discussion

Characterization of the synthesized materials

Fig. 1a shows the TEM of 3D ZnO, which has a sea urchin-like microstructure consisting of a large number of one-dimensional (1D) nanorods. These nanorods were reoriented toward the same point at the center, with dimensions of about 5 μm and diameters in the range of 300–500 nm. As shown in Fig. 1b, the SEM images further demonstrated that the sea urchin-like structure of 3D ZnO is composed of many 1D nanorods with a remarkably smooth surface. The TEM image in Fig. 1c illustrates the uniform reduction of AuNPs on the 3D ZnO surface. Fig. 1d shows the excellent dispersion of AuNPs with a size of 30–60 nm on ZnO. Fig. 1f shows the successful attachment of the g-C_3N_4 nanospheres. The 3D ZnO/Au surface is quite rough due to the attachment of the g-C_3N_4 nanospheres, but they do not change the 3D ZnO morphology significantly (Fig. 1e). The high-resolution transmission electron microscopy (HRTEM) image of 3D ZnO (Fig. 1g) clearly showed an interplanar distance of 0.26 nm, which belongs to the (002) plane of ZnO.[24,25] Fig. 1h shows the HRTEM image of 3D ZnO/Au/g-C_3N_4 captured near the edges of the nanorods; the AuNP (111) crystalline surfaces were tightly attached to the surface of the ZnO nanorods.[26]

Energy-dispersive X-ray spectroscopy (EDX) (Fig. S2†) revealed the content of each element in the composite. The characteristic peak intensity was the strongest for Zn, second highest for O, and weaker for Au, C, and N. The reason is that ZnO is the main component in the composite. As shown in Fig. S3,† the crystalline phases and crystallinity of 3D ZnO, 3D ZnO/Au, g-C_3N_4, 3D ZnO/g-C_3N_4 and 3D ZnO/Au/g-C_3N_4 were determined by X-ray diffraction (XRD). In comparison

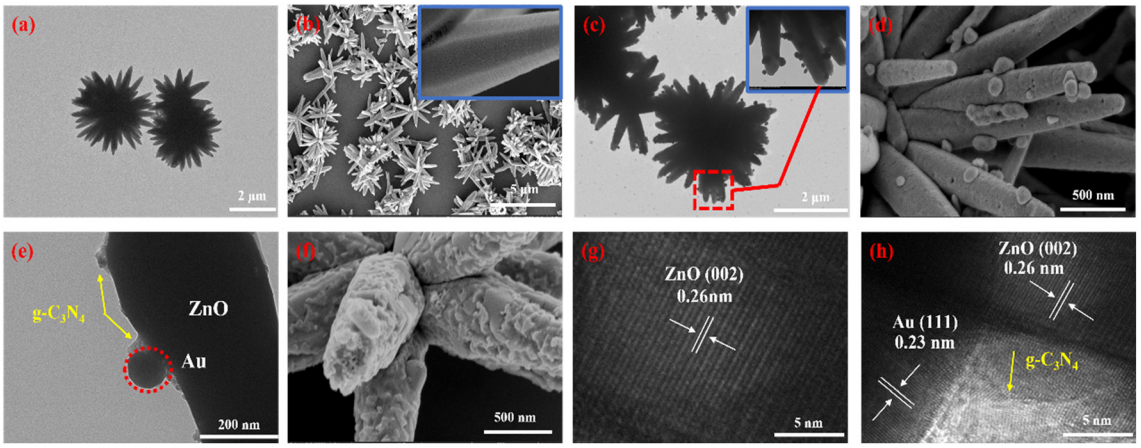

Fig. 1 The TEM and SEM images of (a and b) 3D ZnO, (c and d) 3D ZnO/Au and (e and f) 3D ZnO/Au/g-C_3N_4, respectively. The HRTEM images of (g) 3D ZnO and (h) 3D ZnO/Au/g-C_3N_4.

with the other materials (Fig. S3a†), 3D ZnO/Au/g-C_3N_4 (purple curve) not only presented the characteristic diffraction peak of ZnO but also exhibited the characteristic peak of Au. After the vapour phase deposition of g-C_3N_4, the characteristic peak belonging to g-C_3N_4 (27.5°) also appeared in the pattern (Fig. S3b†). This further supports the highly crystalline nature of the prepared material. The states of the elements in the composite were studied by X-ray photoelectron spectroscopy (XPS) measurements. As shown in Fig. S4a,† the two main peaks in the C1s spectrum belonged to C–C (285.1 eV) and the sp^2 hybridized carbon in N–C=N (289.2 eV). Similarly, Fig. S4b† shows three characteristic peaks in the N1s spectrum corresponding to C–N=C (398.5 eV), C–N–H (402.6 eV) and C=N (405.3 eV), respectively. The UV-vis absorption spectra confirmed the improved light absorption of 3D ZnO/g-C_3N_4 in both the UV and visible regions at 455 nm compared with pristine ZnO due to the g-C_3N_4 modification (Fig. S5†).

Performance of the PEC electrode

As shown in Fig. 2a, both 3D ZnO and g-C_3N_4 exhibited low photocurrents due to the recombination of photoinduced carriers. However, the combination of 3D ZnO and g-C_3N_4 led to significantly enhanced photocurrent due to the construction of heterojunctions. When AuNPs were introduced to form 3D ZnO/Au/g-C_3N_4, the photoelectrode showed the highest photocurrent response, approximately four times that of pristine 3D ZnO and twice that of 3D ZnO/g-C_3N_4.

To investigate the possible mechanism underlying the changing photocurrent of the system, the corresponding reflectance of ZnO and g-C_3N_4 was obtained through UV-vis DRS measurements (as detailed in Fig. S6†). The calculated bandgap was 3.11 eV for ZnO (Fig. S6a†) and 2.77 eV (*versus* vacuum energy (E_{vac})) for g-C_3N_4 (Fig. S6b†). Obviously, ZnO has a wider band gap. Thus, the formation of heterojunction between ZnO and g-C_3N_4 is possible. As displayed in Fig. S7 in ESI,† the values of the Fermi level (E_f) of ZnO and g-C_3N_4 were 1.94 eV and 1.76 eV E_{vac}, which were calculated using the ultraviolet photoelectron spectroscopy (UPS) work function derived from the excitation energy (HeI, 21.2 eV), and the VB edge (E_{vb}) values for ZnO and g-C_3N_4 were 7.32 eV and 6.80 eV *versus* E_{vac}, respectively. Furthermore, the CB energies (E_{cb}) of ZnO and g-C_3N_4 were determined to be 4.21 eV and 4.03 eV *versus* E_{vac}, respectively (based on the equation: $E_{cb} = E_{vb} - E_g$). The values of E_{vb} and E_{cb} of ZnO and g-C_3N_4 were corresponding to 2.88 eV, 2.35 eV, −0.23 eV and −0.42 eV *versus* RHE, respectively. Fig. 2b shows the energy band arrangement of ZnO and g-C_3N_4 before and after the formation of the composite. Due to their complexation, the g-C_3N_4 energy band edge bends upward, and the ZnO energy band edge bends downward.[27] From the bandgap positions of ZnO and g-C_3N_4, it can be inferred that only a type-II heterojunction or Z-scheme heterojunction can be formed between them.

The mechanism of the proposed Z-scheme heterojunction was verified using photoluminescence (PL). Typically, the photocatalyst (2 mg) was dispersed in an aqueous solution (5 mL) of 0.5 mM terephthalic acid and 2 mM NaOH. It was irradiated with a 300 W xenon lamp for 1 h and sampled and analyzed on an EI FLS980 spectroscopy test system with an excitation wavelength of 320 nm. The use of terephthalic acid as a probe molecule is attributed to the fact that hydroxyl radicals (˙OH) produced on the surfaces of 3D ZnO, pure g-C_3N_4, ZnO/g-C_3N_4 and ZnO/Au/g-C_3N_4 can be detected by terephthalic acid. Therefore, PL detection was carried out under the light. Fig. S8 in ESI† shows the comparative PL results of 3D ZnO, g-C_3N_4, ZnO/g-C_3N_4 and ZnO/Au/g-C_3N_4 after 1 h of illumination. All samples had a strong PL signal at 425 nM, indicating that ˙OH were produced on their surfaces. This is attributed to the energy band positions of ZnO and g-C_3N_4 with the OH^-/˙OH (2.8 V *vs.* NHE) and O_2/O_2^- (−0.3 V *vs.* NHE) standard redox potentials, which suggests that the photogenerated holes from the VB of ZnO produce ˙OH directly and the photogenerated electrons from the CB

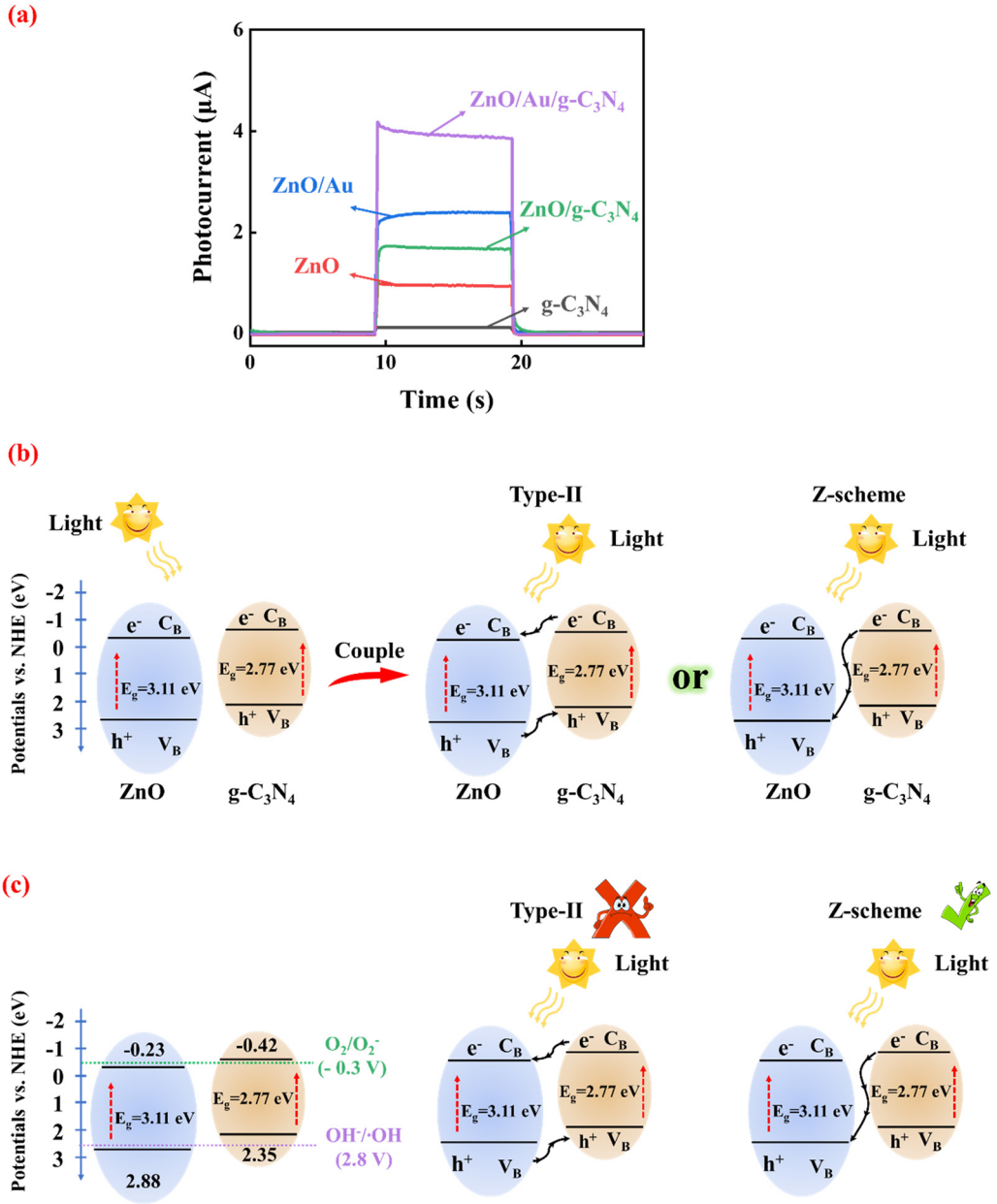

Fig. 2 (a) The photocurrent response of different electrodes. (b) The possible types of heterojunctions resulting from the coupling of ZnO and g-C_3N_4. (c) The band edge positions of g-C_3N_4 and 3D ZnO and the standard redox potentials of the OH^-/·OH and O_2/O_2^- couples.

of g-C_3N_4 also produce ·OH but indirectly by deriving it from superoxide radicals (O_2^-).[28] As shown in Fig. 2c, ·OH and O_2^- cannot be detected if a type-II heterojunction is formed. ZnO/g-C_3N_4 exhibited a stronger PL intensity than ZnO and g-C_3N_4, which indicates that more ·OH was produced by ZnO/g-C_3N_4. It is well-known that Z-scheme heterojunctions have stronger redox ability. Therefore, ZnO/g-C_3N_4 supported sufficient oxidation to generate ·OH and sufficient reduction to generate O_2^-. In addition, ZnO/Au/g-C_3N_4 showed the strongest PL intensity signal because the LSPR effect of the AuNP intermediates effectively promotes carrier transfer between ZnO and g-C_3N_4. According to the experimental results of PL, the charge carrier transfer in the ZnO/Au/g-C_3N_4 composite photocatalysis system matches the direct Z-scheme type than type-II semiconductors, which is consistent with our inference. Under xenon lamp irradiation, the photogenerated carriers are accelerated by transport across the Z-scheme heterojunction. The charge transfer is greatly enhanced, which is responsible for the significant increase in photocurrent intensity.

The principle of GSH detection by the PEC biosensor

GSH, which is a reducing substance, has the potential to serve as a hole scavenger. The principle of GSH sensing based on the 3D ZnO/Au/g-C_3N_4 heterostructure is shown in

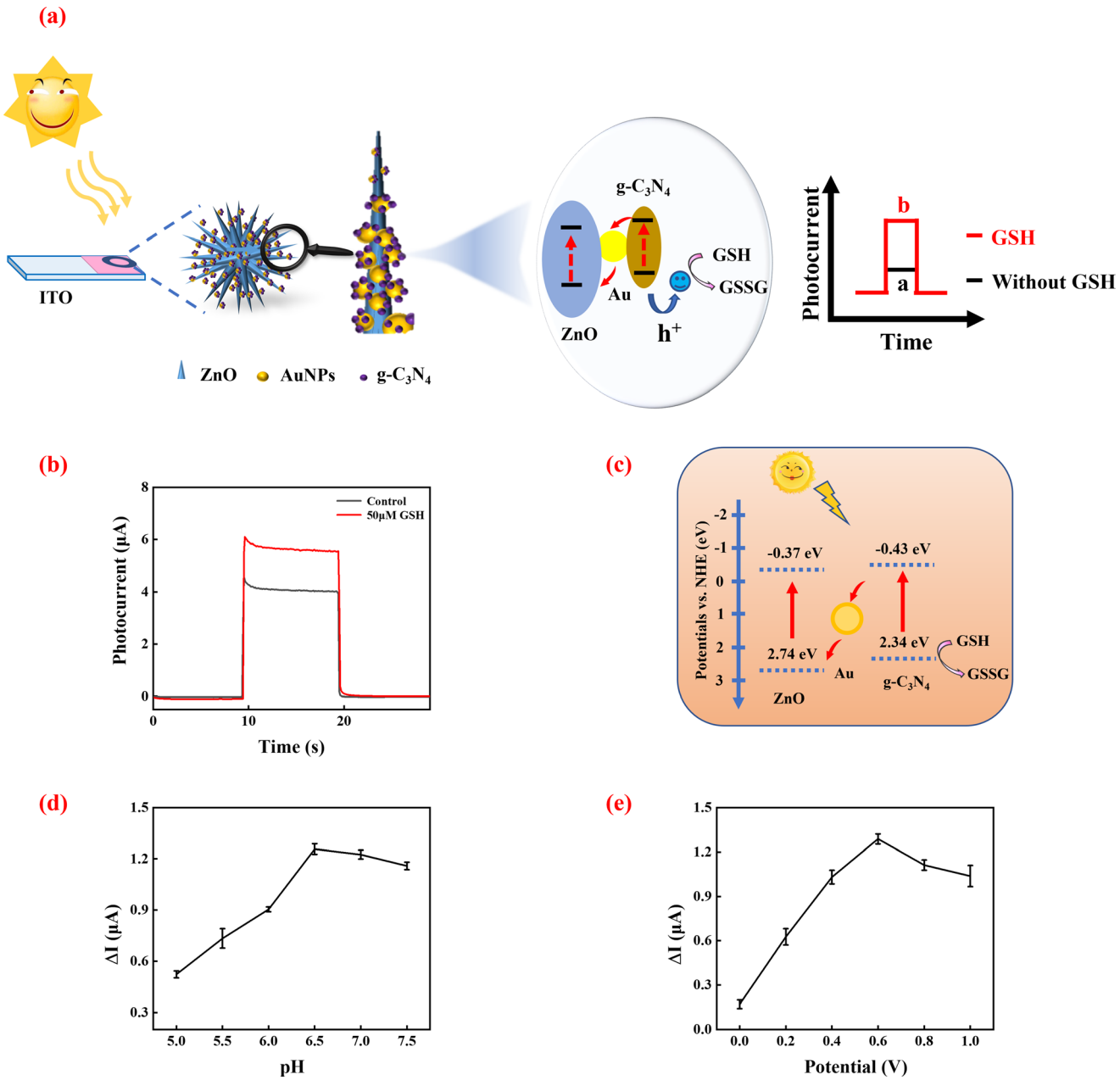

Fig. 3 (a) The schematic of the principle of GSH detection by the PEC biosensor. (b) The PEC response of 3D ZnO/Au/g-C_3N_4 in the presence and absence of GSH. (c) The schematic of the carrier transfer in the 3D ZnO/Au/g-C_3N_4 ternary heterojunction under illumination. The effect of (d) pH and (e) bias voltage on the photocurrent of the system.

Fig. 3a. The electrons of GSH eliminate the photogenerated holes in the VB of g-C_3N_4, which prevent the rapid recombination of photogenerated electron–hole pairs in 3D ZnO/Au/g-C_3N_4. This results in the enhancement of the photocurrent detected. As the GSH concentration increases, more photogenerated holes are consumed, and the photocurrent rises accordingly. Based on this, it is possible to develop a sensitive PEC biosensor for GSH detection.[23]

To verify the feasibility of the above sensing strategy, a simple PEC test was first performed. As shown in Fig. 3b, 3D ZnO/Au/g-C_3N_4 exhibited a high photocurrent intensity response. The system photocurrent was enhanced obviously after the addition of GSH. The reason is that GSH can be oxidized by holes as it is an electron donor, which effectively reduces the recombination of photogenerated electron–hole pairs, leading to enhanced photocurrent. These results demonstrate the feasibility of the sensor built using the 3D ZnO/Au/g-C_3N_4 heterojunction for GSH detection.

Fig. 3c shows a schematic of the charge transfer at the 3D ZnO/Au/g-C_3N_4 heterojunction when GSH is added to the

system. When 3D ZnO/Au/g-C_3N_4 is exposed to the xenon lamp, ZnO and g-C_3N_4 are excited simultaneously, producing electron–hole pairs, respectively.

Under illumination,

$$ZnO/Au/g\text{-}C_3N_4 + h\nu \rightarrow h^+ + e^- \quad (1\text{-}1)$$

At the photoanode,

$$H_2O + 2h^+ \rightarrow 1/2O_2 + 2H^+ \quad (1\text{-}2)$$

At the Pt electrode,

$$2H^+ + 2e^- \rightarrow H_2 \quad (1\text{-}3)$$

The Z-scheme heterojunction promotes fast transport of the photogenerated carriers. AuNPs act as mediators and also facilitate photoelectron transfer from ZnO to g-C_3N_4. When GSH is present in the system, GSH acts as a hole scavenger and effectively slows down the complexation of the electron–hole pairs so that a stronger photocurrent can be detected.

Under illumination,

$$ZnO/Au/g\text{-}C_3N_4 + h\nu \rightarrow h^+ + e^- \quad (2\text{-}1)$$

At the photoanode,

$$GSH + 2h^+ \rightarrow GSSG + 2H^+ \quad (2\text{-}2)$$

At the Pt electrode,

$$2H^+ + 2e^- \rightarrow H_2 \quad (2\text{-}3)$$

Optimization of the experimental conditions

To achieve the best GSH sensing performance, some parameters of the system were optimized. GSH solutions are susceptible to oxidation, which is influenced by temperature, pH, light and other conditions, producing oxidized glutathione. pH is a crucial factor, which affected the performance of the GSH assay greatly. As shown in Fig. 3d, the enhanced photocurrent ($\Delta I = I - I_0$, where I_0 is the photocurrent intensity value for the blank group (without GSH), and I is the photocurrent intensity value in the presence of 50 μM GSH) gradually increased with the pH from 5.0 to 6.5. When the pH was higher than 6.5, the enhanced photocurrent began to decrease gradually, which is attributed to the fact that GSH can be easily oxidized to form oxidized glutathione (GSSG), and GSSG cannot provide electrons that neutralize the holes in the VB of g-C_3N_4. Therefore, the pH of the assay was determined to be 6.5.

The effect of bias potential was also optimized. As shown in Fig. 3e, ΔI increased with increasing bias potential and reached a maximum value at 0.6 V. Then, ΔI gradually decreased when the bias potential was further increased to 1.0 V. This is because, under certain conditions of the incident light, the bias increases the kinetic energy of the photoelectrons and results in the enhancement of the photocurrent. However, the photocurrent is limited by the number of photoelectrons and will not increase further. Therefore, 0.6 V was chosen as the optimum potential.

The performance of the biosensor

As shown in Fig. 4a, under optimized conditions, the measured photocurrent signal increased with increasing GSH concentration. Fig. 4b shows that there was a linear relationship between ΔI and the logarithm of target concentration between 7 and 2000 μM. The linear equation (as in eqn (3)) was

$$\Delta I = 1/11 \lg C_{GSH} - 0.71 \quad R^2 = 0.9984 \quad (3)$$

where C_{GSH} is the concentration of GSH in the sample, and R is the linear correlation coefficient. The limit of detection (LOD) was 2.3 μM (LOD = $3S/K$, K is the slope of the calibration curve, and S is the standard deviation of the blank).

Photocurrents in the presence of various interfering substances (*e.g.* metal ions, common chemical and biological samples) were measured to verify the selectivity of the sensor. The concentration of GSH was 50 μM, while the concentration of the interfering agent was 500 μM. As shown in Fig. 4c, compared with GSH, much smaller responses were detected in the presence of the interfering molecules. Although high concentrations of Glu and Arg could also produce a PEC response in the system, their levels (μM levels) in biological systems are much lower than that of GSH (mM levels).[29,30] Therefore, these compounds will not cause a great interference to GSH detection in real samples.

The stability of the sensor is shown in Fig. 4d. There was no significant change in photocurrent intensity after 10 cycles of on/off irradiation in the absence and presence of 50 μM GSH, signifying that the sensor has excellent stability. To explore the reproducibility of the sensor, five independent tests were performed at 50 μM GSH, and the relative standard deviation (RSD) of the measured photocurrent intensity was 4.9%, showing that the constructed sensing platform has excellent reproducibility.

The performance of the proposed PEC sensor was compared with other GSH detection methods (Table S1†). The results showed the superior performance of this method with a wider linear range and a relatively lower LOD. This can be attributed to the development of a multi-component high-sensitivity PEC platform by the modification of the 3D ZnO surface using AuNPs and g-C_3N_4. Using the sea urchin-like, surface plasmon resonance effect and the synergistic effect of the Z-scheme heterojunction, the carrier separation and transfer are greatly enhanced, and more holes are trapped by GSH as a hole scavenger.

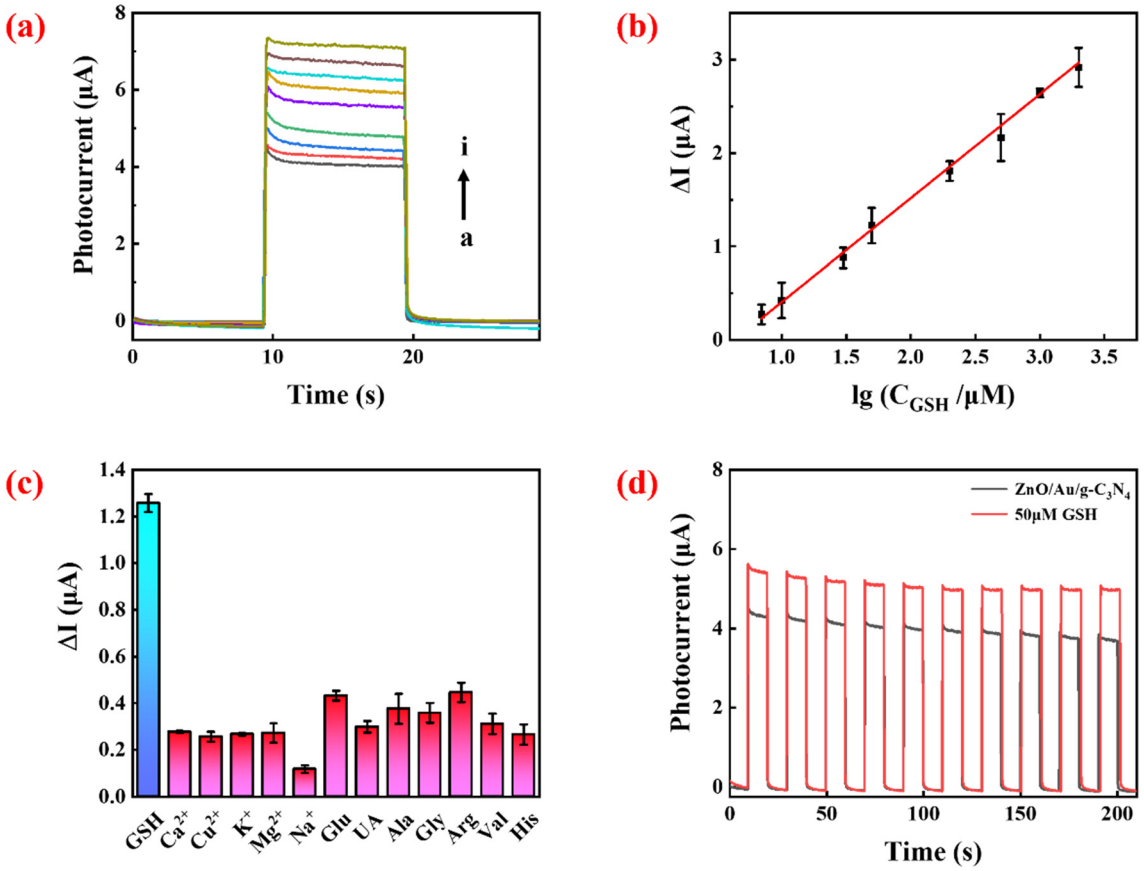

Fig. 4 (a) The photocurrent of the system after the addition of different concentrations of GSH. From a to i: 0, 7, 10, 30, 50, 200, 500, 1000 and 2000 μM. (b) The linear relationship between the change in photocurrent intensity and the logarithmic concentration of GSH. (c) The response of the sensor to GSH (50 μM) *versus* other interfering substances (500 μM). (d) The photocurrent response over 10 on/off light cycles in the presence and absence of 50 μM GSH.

Real samples analysis

To assess the practical application of the proposed biosensor, GSH in three real serum samples (donated by volunteers from the Affiliated Hospital of Putian University, China) was detected, and spiked recovery experiments were carried out. This study was approved by the local ethics committee of the First Affiliated Hospital of Putian University and compliant with the Declaration of Helsinki (2008). Written informed consent was obtained from all participants. The results are shown in Table 1. The spiked recoveries ranged from 98.9% to 110.5%, and the relative standard deviations of the three parallel independent experiments ranged from 1.7% to 4.8%. This demonstrates the potential of the sensor in practical sample detection.

Table 1 Application of the constructed PEC sensor to detect GSH in human serum (n = 3)

Samples	Added (μM)	Found (μM)	Recovery (%)	RSD (%)
1	0	28.5	—	3.1
	10	38.8	102.4	2.3
	100	139.0	110.5	2.6
	1000	1064.5	103.6	2.2
2	0	24.4	—	1.9
	10	34.5	101.0	2.6
	100	131.7	107.3	3.2
	1000	1093.4	106.9	4.1
3	0	22.9	—	1.7
	10	33.4	105.0	2.9
	100	121.8	98.9	4.8
	1000	1022.1	99.9	3.6

Conclusion

In this study, a Z-scheme 3D ZnO/Au/g-C_3N_4 heterojunction photoelectrode was designed, and it exhibited significantly enhanced photocurrent because of the following unique advantages: (1) the 3D sea urchin-like structure composed of nanorods provided a directional channel for fast carrier transport and abundant reaction sites; (2) the Z-scheme has a stronger redox ability along with more efficient charge transfer and separation; (3) the AuNPs sandwiched between 3D ZnO and g-C_3N_4 act as mediators and greatly reinforce vector electron transfer in the Z-scheme heterojunction. GSH was chosen as the model target to test the potential application of the designed photoelectrode. The proposed

system shows satisfactory results in the specific detection of GSH in serum samples.

Author contributions

Weixin Li: investigation, data curation, writing – original draft. Xinyang Wang: software, methodology. Jiaji Huang: resources, software. Min Zhao: resources, software. Jiao Yang: data curation. Fang Luo: resources, software. Bin Qiu: resources. Jian Wang: resources, software. Zhenyu Lin: writing-review & editing, project administration, funding acquisition.

Conflicts of interest

The authors declare that they have no known competing financial interests or personal relationships that could have appeared to influence thee work reported in this paper.

Acknowledgements

The authors gratefully acknowledge the financial support of the National Sciences Foundation of China (21974020).

References

1 Y.-T. Xu, S.-Y. Yu, Y.-C. Zhu, G.-C. Fan, D.-M. Han, P. Qu and W.-W. Zhao, *TrAC, Trends Anal. Chem.*, 2019, **114**, 81–88.
2 W. W. Zhao, J. J. Xu and H. Y. Chen, *Anal. Chem.*, 2018, **90**, 615–627.
3 R. M. Hewlett and M. A. McLachlan, *Adv. Mater.*, 2016, **28**, 3893–3921.
4 Z. Wang, M. Cao, L. Yang, D. Liu and D. Wei, *Analyst*, 2017, **142**, 2805–2811.
5 J. Tang, B. Kong, Y. Wang, M. Xu, Y. Wang, H. Wu and G. Zheng, *Nano Lett.*, 2013, **13**, 5350–5354.
6 J. Elias, C. Levy-Clement, M. Bechelany, J. Michler, G. Y. Wang, Z. Wang and L. Philippe, *Adv. Mater.*, 2010, **22**, 1607–1612.
7 X. Ren, A. Sangle, S. Zhang, S. Yuan, Y. Zhao, L. Shi, R. L. Hoye, S. Cho, D. Li and J. L. MacManus-Driscoll, *J. Mater. Chem. A*, 2016, **4**, 10203–10211.
8 J. Low, J. Yu, M. Jaroniec, S. Wageh and A. A. Al-Ghamdi, *Adv. Mater.*, 2017, **29**, 1601694.
9 H. Wang, L. Zhang, Z. Chen, J. Hu, S. Li, Z. Wang, J. Liu and X. Wang, *Chem. Soc. Rev.*, 2014, **43**, 5234–5244.
10 Y. Zhou, H. Yin and S. Ai, *Coord. Chem. Rev.*, 2021, **447**, 214156.
11 S. Patnaik, D. P. Sahoo and K. Parida, *Carbon*, 2021, **172**, 682–711.
12 S. S. Low, Z. Chen, Y. Li, Y. Lu and Q. Liu, *TrAC, Trends Anal. Chem.*, 2021, **145**, 116454.
13 Š. Hajduk, S. P. Berglund, M. Podlogar, G. Dražić, F. F. Abdi, Z. C. Orel and M. Shalom, *Adv. Mater. Interfaces*, 2017, **4**, 1700924.
14 X. Geng, L. Wang, L. Zhang, H. Wang, Y. Peng and Z. Bian, *Chem. Eng. J.*, 2021, **420**, 129722.
15 X. Liang, J. Zhao, T. Wang, Z. Zhang, M. Qu and C. Wang, *ACS Appl. Mater. Interfaces*, 2021, **13**, 33034–33044.
16 Y. Fu, Z. Ren, J. Wu, Y. Li, W. Liu, P. Li, L. Xing, J. Ma, H. Wang and X. Xue, *Appl. Catal., B*, 2021, **285**, 119785.
17 K. Leng, W. Mai, X. Zhang, R. Liu, X. Lin, J. Huang, H. Lou, Y. Xie, R. Fu and D. Wu, *Chem. Commun.*, 2018, **54**, 7159–7162.
18 N. Zhang, S. Xie, B. Weng and Y.-J. Xu, *J. Mater. Chem. A*, 2016, **4**, 18804–18814.
19 C. X. Guo, J. Xie, H. Yang and C. M. Li, *Adv. Sci.*, 2015, **2**, 1500135.
20 C. Zhou, S. Wang, Z. Zhao, Z. Shi, S. Yan and Z. Zou, *Adv. Funct. Mater.*, 2018, **28**, 1801214.
21 X. L. Fu, F. Hou, F. R. Liu, S. W. Ren, J. T. Cao and Y. M. Liu, *Biosens. Bioelectron.*, 2019, **129**, 72–78.
22 Q.-X. Sun, S.-Q. Zhang, X. Wei, T. Yang, J.-H. Wang and M.-L. Chen, *Anal. Chim. Acta*, 2022, **1221**, 340100.
23 D. Liu, X. Bai, J. Sun, D. Zhao, C. Hong and N. Jia, *Sens. Actuators, B*, 2022, **359**, 131542.
24 R. Lv, T. Wang, F. Su, P. Zhang, C. Li and J. Gong, *Nano Energy*, 2014, **7**, 143–150.
25 S. S. Patil, M. A. Johar, M. A. Hassan, D. R. Patil and S.-W. Ryu, *Appl. Catal., B*, 2018, **237**, 791–801.
26 Z. Yin, B. Chen, M. Bosman, X. Cao, J. Chen, B. Zheng and H. Zhang, *Small*, 2014, **10**, 3537–3543.
27 Z.-F. Huang, J. Song, X. Wang, L. Pan, K. Li, X. Zhang, L. Wang and J.-J. Zou, *Nano Energy*, 2017, **40**, 308–316.
28 J. W. Jang, S. Cho, G. Magesh, Y. J. Jang, J. Y. Kim, W. Y. Kim, J. K. Seo, S. Kim, K. H. Lee and J. S. Lee, *Angew. Chem., Int. Ed.*, 2014, **53**, 5852–5857.
29 Q. Y. Cai, J. Li, J. Ge, L. Zhang, Y. L. Hu, Z. H. Li and L. B. Qu, *Biosens. Bioelectron.*, 2015, **72**, 31–36.
30 X. Dong, C. Xu, C. Yang, F. Chen, A. G. Manohari, Z. Zhu, W. Zhang, R. Wang, D. You and J. Chen, *J. Mater. Chem.*, 2019, **7**, 5624–5629.